Electron Temperature Inference from Multiple Fixed Bias Langmuir Probes

Florine Enengl[1], Sigvald Marholm[2], Sayan Adhikari[2], Richard Marchand[3], and Wojciech Jacek Miloch[1]

[1]University of Oslo
[2]Institute for Energy Technology
[3]University of Alberta

December 7, 2022

Abstract

We show the first achievement of inferring the electron temperature in ionospheric conditions from synthetic data using fixed-bias Langmuir probes operating in the electron saturation region. This was done by using machine learning and altering the probe geometry. The electron temperature is inferred at the same rate as the currents are sampled by the probes. For inferring the electron temperature along with the electron density and the floating potential, a minimum number of three probes is required. Furthermore does one probe geometry need to be distinct from the other two, since otherwise the probe setup may be insensitive to temperature. This can be achieved by having either one shorter probe or a probe of a different geometry, e.g. two longer and a shorter cylindrical probe or two cylindrical probes and a spherical probe. We use synthetic plasma parameter data and calculate the synthetic collected probe currents to train a neural network and verify the results with a test set. We additionally verify the validity of the inferred temperature in altitudes ranging from about 100 km-500 km, using data from the International Reference Ionosphere model. Even minor changes in the probe sizing enable the temperature inference and result in root mean square relative errors between inferred and ground truth data of under 3%. When limiting the temperature inference to 120-450 km altitude an RMSRE of under 0.7% is achieved for all probe setups. In future, the multi-needle Langmuir Probe instrument dimensions can be adapted for higher temperature inference accuracy.

Electron Temperature Inference from Multiple Fixed Bias Langmuir Probes

F. Enengl[1], S. Marholm[1,2], S. Adhikari[1,2], R. Marchand[3], W.J. Miloch[1]

[1]Department of Physics, University of Oslo, P.O. Box 1048 Blindern, N-0316 Oslo, Norway
[2]Department of Computational Materials Processing, Institute for Energy Technology, Kjeller, Norway
[3]Department of Physics, University of Alberta, Edmonton AB, Canada T6G 2E1

Key Points:

- The electron temperature is inferred in ionospheric conditions from synthetic data using fixed-bias Langmuir probes.
- Electron temperature inference can be achieved from setups of at least three probes, one probe geometry needs to be distinct from the others.
- At an altitude of 120–450 km an RMS relative error of under 0.7% of the inferred temperature is achieved for all probe setups.

Corresponding author: Florine Enengl, `florine.enengl@fys.uio.no`

Abstract

We show the first achievement of inferring the electron temperature in ionospheric conditions from synthetic data using fixed-bias Langmuir probes operating in the electron saturation region. This is done by using machine learning and altering the probe geometry. The electron temperature is inferred at the same rate as the currents are sampled by the probes. For inferring the electron temperature along with the electron density and the floating potential, a minimum number of three probes is required. Furthermore does one probe geometry need to be distinct from the other two, since otherwise the probe setup may be insensitive to temperature. This can be achieved by having either one shorter probe or a probe of a different geometry, e.g. two longer and a shorter cylindrical probe or two cylindrical probes and a spherical probe. We use synthetic plasma parameter data and calculate the synthetic collected probe currents to train a neural network and verify the results with a test set. We additionally verify the validity of the inferred temperature in altitudes ranging from about 100 km–500 km, using data from the International Reference Ionosphere model. Even minor changes in the probe sizing enable the temperature inference and result in root mean square relative errors between inferred and ground truth data of under 3%. When limiting the temperature inference to 120–450 km altitude an RMSRE of under 0.7% is achieved for all probe setups. In future, the multi-needle Langmuir Probe instrument dimensions can be adapted for higher temperature inference accuracy.

1 Introduction

Langmuir probes are commonly used to measure plasma parameters, such as electron density and electron temperature, which can be derived from collected currents. To collect a current, a biased/floating conductor is exposed to a plasma (Mott-Smith & Langmuir, 1926). The probes are used in laboratory and space plasmas (e.g. ionosphere, (Brace, 1998)) and have been flown in various setups on numerous satellite and rocket missions. A common way to operate the probes is to step through a pre-defined set of voltages, whilst measuring the current, and produce a current–voltage graph needed to derive the plasma parameters. A sweep takes multiple time steps to be completed and therefore the parameters are derived at a lower resolution than the actual sampling rate provides. Therefore, the data recorded with high resolution in time and space are not exploited to its full potential. Another option is to have multiple probes operating at a fixed bias, but different from each other. This Langmuir probe sampling concept is used by Jacobsen et al. (2010); Bekkeng et al. (2010), with its aim to measure absolute electron density at a resolution sufficient to resolve finer structures than possible with present techniques in an ionospheric plasma. The electron temperature can not be resolved at the same rate in this sampling concept, it is however an important parameter to characterize plasma. Ionospheric plasma irregularities and instabilities can be driven e.g. by currents, density gradients, drifts, temperature gradients. The electron temperature plays an important role for characterizing irregularities and instabilities in plasma. Various attempts were made to understand which instabilities dominate at different ionospheric conditions (e.g. Fejer & Kelley, 1980; Keskinen & SL, 1983; Onishchenko et al., 2004; Perron et al., 2009, 2013; Moen et al., 2013; Eltrass & Scales, 2014; Dimant et al., 2021; Enengl et al., 2022, and others). To improve our characterization of ionospheric plasma and understand predominant instabilities, the availability of temperature data in sufficient resolution is crucial. Characterization of plasma processes and instabilities is also important in other regions, such as in the Earth's magnetosphere and the solar wind (e.g. Beghin et al., 2017; Yoon, 2017, and others). In this work we aim to provide a method to retrieve the electron temperature with high sampling resolution from fixed-bias Langmuir probe setups, similar to the multi-needle Langmuir probe (m-NLP) setup proposed by Jacobsen et al. (2010); Bekkeng et al. (2010). The m-NLP consists of four cylindrical probes. For sufficiently long probes with small radii, the m-NLP is assumed to operate according to the orbital-motion limited (OML) theory. The theory is valid for a probe radius smaller than the Debye length in an unmagnetized, non-drifting, Maxwellian plasma. The m-NLP setup should then provide a way to measure the plasma density independently of the temperature and the spacecraft's floating potential (Jacobsen et al., 2010). In the electron saturation region the ion current to the probe is negligible and the electron current collected is then given by

$$I_c = n_e q \sqrt{\frac{kT_e}{2\pi m_e}} AC \left(1 + \frac{q(V_f + V_b)}{kT_e}\right)^{\beta} \tag{1}$$

with n_e being the electron density, T_e the electron temperature, $V_f + V_b$ the sum of floating and bias voltage and β is a parameter dependent on the probe geometry and plasma parameters (Mott-Smith & Langmuir, 1926). The parameters q, k, m_e, A are the elementary charge, the Boltzmann constant, the electron mass and the probe surface area respectively. For a cylindrical probe the geometry constant C is $2/\sqrt{\pi}$ and for a spherical probe C is 1, as long as the probe geometries follow the limitations of OML theory.

Jacobsen et al. (2010) assumed β to be 0.5 for two cylindrical probes of 0.51 mm diameter and 25 mm length ($C1$ and $C2$). With this assumption, the temperature dependence is eliminated by taking the difference of the currents squared:

$$I_{c2}^2 - I_{c1}^2 = \cancel{\frac{2kT_e}{m_e}(n_e q 2rl)^2} - \cancel{\frac{2kT_e}{m_e}(n_e q 2rl)^2} + \frac{2q}{m_e}(n_e q 2rl)^2 V_2 - \frac{2q}{m_e}(n_e q 2rl)^2 V_1. \tag{2}$$

It is then easy to solve for n_e. While Jacobsen et al. (2010) assumes β to be 0.5 for cylindrical probes, the β parameter can, in fact, deviate from the assumed value. As a consequence, the dependence of electron density on electron temperature and floating potential is not eliminated. This is then affecting the accuracy of electron density and spacecraft charging determination (Barjatya et al., 2009; Hoang, Røed, et al., 2018). Different approaches were taken to improve the accuracy of inferred plasma parameters, treating β as an unknown parameter. Barjatya et al. (2009) used a nonlinear fit for the parameters n_e, T_e, V_f, β using equation 1 with the currents collected by the four probes. While Hoang, Røed, et al. (2018) similarly used nonlinear and least square fits, Guthrie et al. (2021) inferred plasma parameters with the use of radial basis functions regression. They succeeded in improving the accuracy for inferring the electron density and spacecraft potential. However, none of them provide an electron temperature, as the inferred parameters seem insensitive to it (Barjatya et al., 2009; Hoang, Røed, et al., 2018). Guthrie et al. (2021) concludes only a weak dependence of collected currents on the temperature for these types of probes. All previous attempts to infer temperature from fixed biased multiple Langmuir probes were unsuccessful.

The problem of inferring electron temperature from multiple fixed-bias Langmuir probes remains open. Marholm (2020) points out that in order to solve for a certain parameter, as for the temperature T_e, it is necessary that the characteristic I be sufficiently sensitive to it, and in a way that allow us to separate its effect from that of other parameters such as the floating potential. When $\beta \neq 0.5$, the temperature no longer cancels like in equation 2. However, based on previous unsuccessful attempts at inferring temperature this is apparently not enough. Given that probes of different length correspond to different β parameters, a stronger temperature sensitivity may be introduced by using different probe lengths. In this work, we investigate for which setups a temperature sensitivity is introduced, and whether the electron temperature can be inferred. We then test our hypothesis practically on synthetic data with machine learning methods, evaluate which probe setups may be used to infer electron temperature, and how the m-NLP can be adapted in future missions. This work is divided in theory, methodology, assessment, summary and conclusion sections. The theory section presents how the probes are dependent on the temperature, and how temperature could be calculated analytically if β were known. This section is followed by the methodology section, in which the network used to infer electron temperature from current measurements is introduced and the testing of the system is described. The assessment section compares the different setups and assesses its accuracy and robustness. In the summary and conclusion section, a short recap of the paper is presented along with suggestions for further improvements of m-NLP for the future.

2 Theory

In this section, we show analytically how the collected probe currents of three probes can introduce temperature sensitivity and how we could calculate the electron temperature analytically, if the β parameters were known.

Let us assume a Langmuir probe setup, which consists of three cylindrical probes collecting currents (I_{c1}, I_{c2}, I_{c3}) according to equation 1. Two of the cylindrical probes have the same length ($l_1 = l_2$) and one of them has a shorter length (l_3) compared to the others. This is also reflected in the factors ($\beta_1 = \beta_2$, $\beta_3 > \beta_1$). A sufficiently long cylinder would have a β of 0.5, while a small sphere corresponds to a β of 1. The shorter a cylinder, the more it approaches the β of a sphere due to edge effects. The geometry constants are indicated as C_n and are the same for two probes of the same geometry. The probes are biased with fixed voltages (V_{b1}, V_{b2}, V_{b3}). Higher bias voltages can lead to a larger plasma wakes behind probes. Wake formation behind Debye-scale Langmuir probes in the ionospheric F-region require higher separation of the probes for accurate measurements (Jao et al., 2022). Here, it is assumed that the probes are well separated, and are not affected by one another, by wakes or by their booms. The floating voltage V_f is unknown, and so is the electron temperature T_e and electron density n_e. We can use equation 1 to describe the currents measured by the cylindrical probes. As previously mentioned, this is valid for a non-drifting, collision-less and non-magnetized plasma. The first condition is fulfilled as the thermal speed of the electrons is larger than the speed of a rocket/ spacecraft relative to the plasma. The plasma density in the ionosphere is low, which makes it possible to assume a collision-less plasma, at least for our region of interest, at altitudes above 120 km. Further, the Larmor radius is sufficiently large compared to our probe radii to neglect magnetic field effects (Jacobsen et al., 2010). Dividing I_{c1} by I_{c2} using equation 1 gives:

$$\frac{I_{c1}}{I_{c2}} = \frac{C_1\left(1 + \frac{q(V_f+V_{b1})}{kT_e}\right)^{\beta_1}}{C_1\left(1 + \frac{q(V_f+V_{b2})}{kT_e}\right)^{\beta_1}}. \tag{3}$$

When the terms

$$\eta = \frac{q(V_f + V_b)}{kT_e} \tag{4}$$

are sufficiently large, the relation I_{c1} by I_{c2} can be simplified to:

$$\frac{I_{c1}}{I_{c2}} = \frac{\left(V_f + V_{b1}\right)^{\beta_1}}{\left(V_f + V_{b2}\right)^{\beta_1}}. \tag{5}$$

$I_{c1}, I_{c2}, V_{b1}, V_{b2}$ are known. If, for the moment, we assume β known, we can solve for V_f. Dividing I_{c1} by I_{c3} using the equation 1 for large η (equation 4) we obtain:

$$\frac{I_{c3}}{I_{c1}} = \frac{C_3\left(\frac{q(V_f+V_{b3})}{kT_e}\right)^{\beta_3}}{C_1\left(\frac{q(V_f+V_{b1})}{kT_e}\right)^{\beta_1}} \tag{6}$$

and solved with known β and C for T_e:

$$T_e = \frac{q}{k}\left(\frac{\left(V_f + V_{b3}\right)^{\beta_3}}{\left(V_f + V_{b1}\right)^{\beta_1}}\frac{I_{c1}C_3}{I_{c3}C_1}\right)^{\frac{1}{\beta_3-\beta_1}} \tag{7}$$

Inspecting equations 6 and 7 shows that when we are well in the electron saturation regime (large η), and β_1 is equal to β_3, the temperature term disappears. This means that for inferring the temperature, a difference between β_1 and β_3 is required. The stronger the temperature dependence is, the easier it is to infer the temperature from the probe setup.

Using cylindrical probes of very different lengths, or even introducing a spherical probe, increases the difference in the geometry factor β and makes the setup more temperature sensitive. At the same time, using two of the probes with the same geometry still keeps the possibility of determining the floating potential, as shown in equation 5.

In these equations, only β unknown, otherwise one could now solve for V_f, T_e and then insert in equation 1 to solve for n_e. For given β parameters, the system can be determined analytically with three unknowns (V_f, n_e, T_e) with only the three fixed-biased probes. However, as β is not known to us, we have to use a different method.

3 Methodology

To infer electron temperatures from collected currents, multiple steps are required. The individual steps are visualized in schematic Figures 2, 3, and 4. The first step being the construction of a synthetic data set consisting of synthetic plasma parameters and corresponding currents, see Figure 2. This is used to train a neural network with synthetic training and validation data, which is then evaluated on the synthetic test set, see Figure 3. As a third step, the machine learning model is then applied to data from the International Reference Ionosphere (IRI), used as another test set to further evaluate its performance, see Figure 4. Finally, the model's robustness to noise is tested and its limitations are assessed.

3.1 Construction of Synthetic Plasma Parameter Data Set and Derived Currents

Step 1: A synthetic data set is defined based on plasma parameters that are encountered in the regions of interest. In this study the goal is to infer electron temperature based on data collected in the lower ionosphere (here: 120-500 km). The plasma parameter ranges are selected in accordance with which values the IRI model predict for the region. IRI is an empirical standard model of the ionosphere, based on available data sources (Bilitza, 2018). The electron density values are chosen to be in the range of 4×10^{10} to 3×10^{11} m^{-3}, the electron temperatures are varying from 300 to 2800 K and the floating potential is set to range from -2 to 0 V, see green box in Figure 2. Logarithmically distributed random values for n_e and uniformly random values for the remaining plasma parameters (T_e and V_f) within the given ranges are determined, so the measured current for each of the probes can be calculated. The current is calculated using a finite length model for the cylindrical probe and a finite radius model for the spherical probe. In the OML theory, the probe radius has to be smaller than the Debye length and the plasma particle motion is determined by the probe potential. The finite length/finite radius model is similar to the OML theory, but adapted using theoretical scaling laws and numerical simulations to allow the probe length/ radii to be larger than the Debye length (Laframboise, 1966; Darian et al., 2019; Marholm & Marchand, 2020; Marholm & Darian, 2021). The finite length model also accounts for edge effects on the cylindrical probes. Both models have been extrapolated further to account for higher values of $\eta > 25$, which are encountered in ionosphere, see Figure 1b. The η parameter is dependent on the T_e, V_f and V_b as shown in equation 4) The extrapolation of the finite radius model has been benchmarked with particle in cell simulations using PTetra (a fully kinetic PIC code by Marchand (2012); Marchand and Resendiz Lira (2017)) to confirm its validity. Figure 1a shows an example of a collected normalized current by a sphere with a radius of 0.5 λ_{Debye} according to the OML theory (shown in black), PTetra simulation results (shown in red) and a power law extrapolation of a normalized computed current vs η table by Laframboise (1966) (shown in blue, $\pm 6\%$ in light blue). The normalized current shown in Figure 1a is the collected current I by the sphere that has been normalized by the thermal current $I_{th} = n_e q \sqrt{kT_e/2\pi m_e} A$, dependent on the sphere radius (through the surface area A) and temperature. The PTetra simulations were carried out with a fixed n_e of 10^{11} m^{-3}, a T_e stepping from 500 to 1000 K and a bias voltage between 1 to 10 V in such a way that η spans from 25 to 110. The sphere radius between 0.24 cm to 0.34 cm. The PTetra simulations are within $\pm 6.5\%$ of the power law extrapolation and thus validates it. The power law extrapolation has been used to calculate currents collected by spherical probes in this study. Below 150 km, η increases rapidly due to decreasing temperature, see Figure 1b, and the black dashed horizontal line is at 150 km. For higher biased probes (7.5V) η is 110 at this altitude. Therefore, the extrapolation has been verified up to $\eta = 110$, see black dashed vertical line in Figure 1b, to guarantee reliable current calculations down to at least 150 km. The data used in Figure 1b is from the IRI database and a floating potential is calculated as described in section 3.3. The whole generated data set consisting of probe geometry, plasma parameters (green box in Figure 2) and corresponding currents (yellow box in Figure 2) is referred to as synthetic data. The data are split into a training, validation and test sets for Step 2 (blue box in Figure 2).

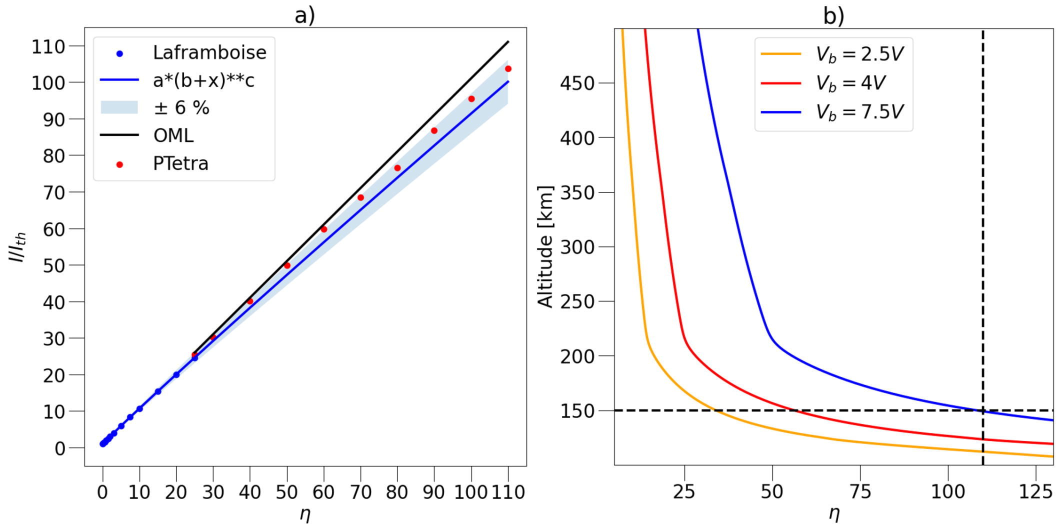

Figure 1. Panel a: Power law extrapolation (blue line) of computed values for the attracted species current (blue dots) from Laframboise (1966), compared with the collected current from the OML theory (black line), PTetra simulations (red dots) as collected by a sphere with a radius of 0.5 λ_{Debye} for η values up to 110. Panel b: Comparison of altitude vs η values for different set bias voltages. The black dashed vertical line at $\eta = 110$ shows how η rapidly increases under an altitude of 150 km (indicated by a black dashed horizontal line). For the main three bias voltages used (2.5,4,7.5V) in this paper, verification of the power law extrapolation up to $\eta = 110$ verifies our current calculations for down to at least 150 km.

3.2 Inferring the Electron Temperature from Probe Currents Using a Neural Network

Now we are fully equipped with a synthetic data set consisting of the necessary parameters (T_e and I). Inverting the relationship between the probe currents and the electron temperature, as shown in equation 7, leaves us with an undetermined system of equations, as the geometry parameters β remain unknown. However, β is not needed when

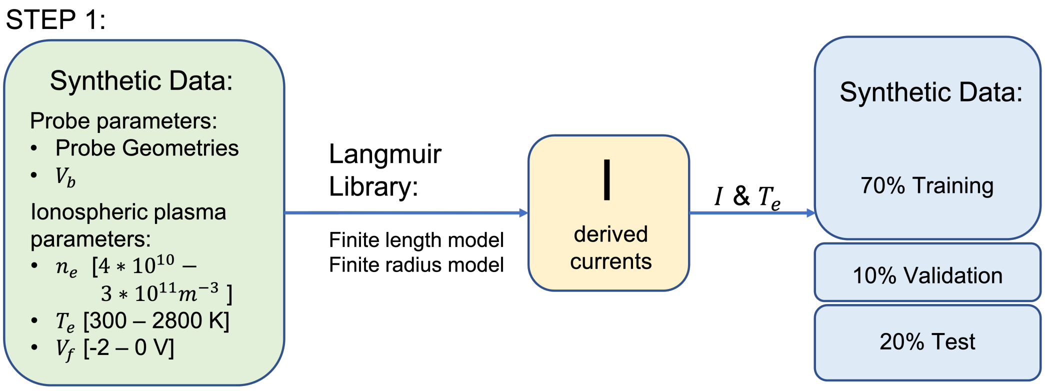

Figure 2. Visualization of Step 1: Construct the synthetic data set (green box), to then derive currents (yellow box) using the Langmuir library finite length and finite radius model and creating the combined synthetic data set of ionospheric plasma parameters and collected currents (blue box).

using the finite-length/finite-radius models to calculate the currents in the synthetic data sets. Machine learning techniques are then applied to invert those models, and infer the temperature. For this we have to construct a neural network (NN), which typically consists of an input layer, multiple hidden layers and an output layer. Every node j in a layer i is assigned a value $v_{i,j}$. The next layer is dependent on the previous layer through weight factors $\omega_{i,j,k}$, activation function a and bias terms $b_{i,j}$ with

$$v_{i+1,k} = \sum_{j=1}^{n_i} \omega_{i,j,k} a(v_{i,j} + b_{i,j}) \tag{8}$$

The network is a type of feed-forward neural network (Goodfellow et al., 2016). First, the input currents are normalized using a preprocessing normalization built-in TensorFlow function. This layer is followed by two dense layers, which use the activation function Rectified Linear Unit (RELU – a standard TensorFlow activation functions from Keras). Both of the dense layers are equipped with 80 nodes/units (dimension of output space). A last dense layer with RELU activation and a single node is used as an output layer. This gives a total number of 7,041 trainable parameters. To compile our NN, the mean absolute error function is chosen in combination with adaptive moment estimation (ADAM) optimizer, both are standard functions from Keras and effective across a wide range of learning methodologies (Kingma & Ba, 2014). The synthetic data set defined in the first step is chosen to consist of at least 13000 combinations of currents and plasma parameters. Of these, 70 % are used for training, 10 % for validation and 20 % for testing, see blue box in Figure 2 and 3). The validation data is used to prevent overfitting, and to understand after how many training steps the model converges (training accuracy and validation accuracy decreasing). The NN (see turquoise box in Figure 3) is first applied to the training and validation set. The training process converges after approximately 80 steps (before the validation accuracy increases). The test set is a separate set, that is not seen during the training. Once the NN has been trained, the machine learning model (see pink box in Figure 3) is stored and applied to the test data. The performance is evaluated by calculating the root mean square relative error (RMSRE) and Pearson correlation coefficient (PCC) between inferred data and synthetic ground truth data, see red box in Figure 3).

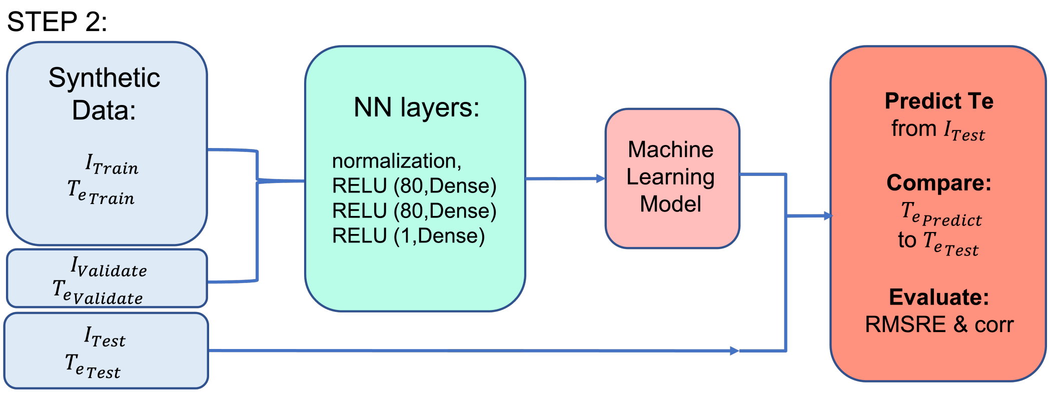

Figure 3. Visualization of Step 2: Use the training and validation data (blue) from Step 1 to train a NN (turquoise box) and save a machine learning model (pink box). Use then the test data current (blue box) from Step 1 and apply the machine learning model (pink) to it. Finally, evaluate the performance of the inferred temperatures compared to the ground truth temperature (red box).

3.3 Evaluation and Robustness of the Model

To evaluate the temperature inference performance further, the machine learning model is applied to another test set, an altitude profile of plasma parameters from IRI. A random altitude profile with electron temperature and electron density values is fetched from the IRI data base, see green box in Figure 4. For the floating potential, we use a current as predicted by OML theory for a sphere, which is dependent on the voltage, and find the voltage where the sum of electron and ion current equals zero by means of a numerical root finder. This voltage is used as the floating potential. This will not be a true floating potential, but it gives us a variable potential that we can use to test our model. For an updated probe design, this should be adjusted to a more realistic value dependent on the probe application environment. The current measured by the probes is then calculated using the same approach as in step 1, using the finite length and finite radius function (see yellow box in Figure 4). On the calculated currents, the machine learning model from step 2 (see pink box in Figure 4) is applied to infer the temperature, which is then compared to the one from IRI to, again, assess the performance of our model by calculating the RMSRE and PCC between inferred data and ground truth IRI data (see red box in Figure 4). Subsequently, we test the model robustness. The robustness is tested by adding shot noise to the input currents also calculated based on IRI data (see yellow box in Figure 4). The added noise is proportional to the square root of the signal strength I_0. The expression for the collected current and corresponding noise I_σ is given by:

$$I_\sigma = I_0 + \sigma\sqrt{|I_0|}r, \tag{9}$$

with σ as a relative standard deviation and r as a random number with a standard Gaussian normal distribution (Ikezi et al., 1968; G. Liu & Marchand, 2021; Marholm & Darian, 2021). The RMSRE and PCC between inferred data and ground truth IRI data is assessed for different levels of noise. As a consistency check, the currents calculated from the synthetic data are compared to currents which are again calculated from the inferred parameters using the finite-length/finite-radius models, as suggested by (G. Liu et al., 2022). This verifies the results of the inference model, as the back-inferred currents should agree with the currents from the synthetic data. The consistency check succeeded, as the currents could be reproduced, but is not shown in this paper. Lastly, we verify that it is still possible to infer the electron density and floating potential from the different probe set-ups.

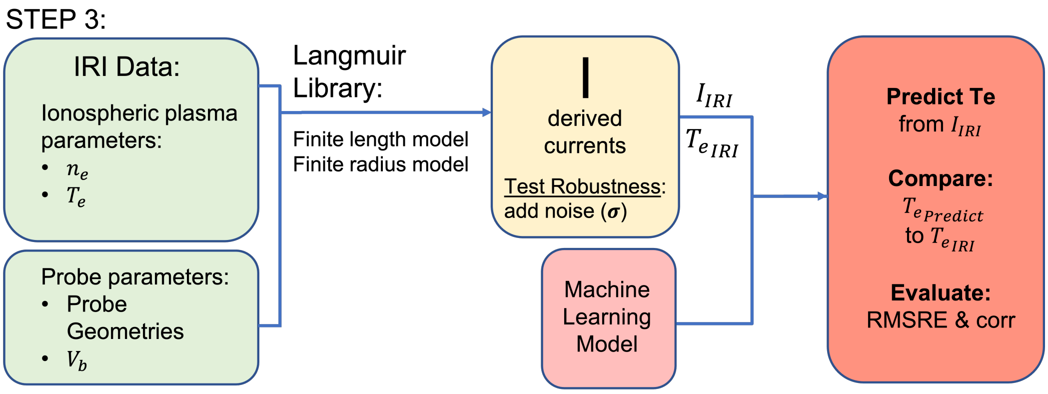

Figure 4. Vizualisation of Step 3: Use another data source (here from IRI) (green box) to derive measured currents (yellow box) to test the machine learning model on (pink box). Evaluate again the inferred temperatures compared to the ground truth (here IRI) temperatures (red box). To test the robustness, add different noise levels to the derived current (yellow box), according to equation 9.

4 Results and Assessment

In this section, three different setups of multiple fixed-bias Langmuir probes are introduced and assessed in their performance of temperature inference. Setup 1 consists of three cylinders, setup 2 of three spheres and setup 3 of a combination of four cylinders and a sphere. As mentioned in section 2, one of the probes in each setup has to be of a different length from the others to increase temperature sensitivity into the system and with that, enable temperature inference. To better quantify the dependence on β, we investigate for the three setups different cases with varied probe length and radius. Limitations and errors for the different cases are given and discussed. The robustness of setups is evaluated by adding noise. Lastly, the inference of floating potential and electron density is demonstrated.

4.1 Setups

The chosen parameters, cylinder length l_n, cylinder radius r_c, sphere radius r_s, bias voltage V_b, for each setup and discussed case are given in table 1, 2 and 3. The expression for the collected current, equation 1, was used to analytically calculate values for β for each set of selected synthetic plasma parameters, probe parameters and constants. This equation is based on OML theory assumptions, however it still provides an approximate value for β. The mean value and standard deviation of β for each probe was calculated and is stated in tables 1, 2 and 3. β varies for different geometries and is also dependent on the plasma parameters and slightly on the bias voltage. This is why there is a deviation of β over the altitude profiles. The difference between β_1 of probe 1 and β_2 of probe 2 is listed as $\Delta\beta$ for each case. This makes it possible to compare the effect of different probe length/β to the performance of the temperature inference. This performance is evaluated by using the RMSRE and the PCC between the test set synthetic electron temperatures and the inferred electron temperatures. The performance param-

Table 1. Parameters for Probe Setup 1: three cylindrical probes. The probes have following bias voltages: V_{b1}=4V,V_{b2}=2.5V,V_{b3}=7.5V. The probe radii r_c are 0.255mm. In the table the probe length (l), geometry factor (β), difference between $\beta_1$and β_2 ($\Delta\beta$) and parameters to evaluate the temperature inference performance RMSRE and PCC are reported.

l_1[cm]	β_1	$l_2 = l_3$[cm]	β_2	β_3	$\Delta\beta$	RMSRE [%]	PCC
2.5	0.73 ± 0.03	3	0.7 ± 0.03	0.73 ± 0.03	0.03	4.3	0.99
2.5	0.73 ± 0.02	4	0.67 ± 0.03	0.71 ± 0.03	0.06	2.4	1
1	0.76 ± 0.01	9	0.6 ± 0.03	0.63 ± 0.03	0.16	0.7	1

Table 2. Parameters for Probe Setup 2: three spherical probes. The probes have following bias voltages: V_{b1}=4V,V_{b2}=2.5V,V_{b3}=7.5V. In the table the probe length (l), geometry factor (β), difference between $\beta_1$and β_2 ($\Delta\beta$) and parameters to evaluate the temperature inference performance RMSRE and PCC are reported.

r_{s1}[cm]	β_1	$r_{s2} = r_{s3}$[cm]	β_2	β_3	$\Delta\beta$	RMSRE [%]	PCC
0.5	0.97 ± 0.03	1.5	0.88 ± 0.07	0.86 ± 0.07	0.08	1.4	1

Table 3. Parameters for Probe Setup 3: four cylindrical probes and one spherical probe. The probes have following bias voltages: V_1=4V,V_2=2.5V,V_3=4V,V_4=5.5V,V_5=10V. In the table the probe length (l), geometry factor (β), difference between $\beta_1$and β_2 ($\Delta\beta$) and parameters to evaluate the temperature inference performance RMSRE and PCC are reported.

r_s[cm]	β_1	l_n[cm]	β_2	$\Delta\beta$	RMSRE[%]	PCC
1	0.92 ± 0.05	2.5	0.72 ± 0.03	0.2	79	0.85
1	0.92 ± 0.05	7	0.62 ± 0.03	0.3	22	0.99
3	0.75 ± 0.09	2.5	0.72 ± 0.03	0.0326	2.5	0.99
0.3	0.99 ± 0.01	2.5	0.72 ± 0.03	0.27	0.8	1

eters are listed in the last two columns of tables 1, 2 and 3. β_2 and β_3 are slightly different due to a difference in bias voltage (all else being equal).

The inferred temperatures as compared to the synthetic test set (ground truth) ones are plotted against each other to visualize the performance in scatter plots such as in Figure 5 a,c,e. The probe geometry parameters, RMSRE is repeated in the plots. The machine learning model was also applied to currents derived from the IRI dataset (used as an additional test set). The inferred temperatures versus the IRI ground truth temperatures are visualized in plots such as in Figure 5 b,f,d, with the RMSRE reported in the plots. The ground truth temperatures are shown in blue, and the predicted/inferred temperatures are shown in orange. The red horizontal lines indicate the range (120–450 km) within which the RMSRE is calculated for. This range has been chosen, as also weaker setups (see Figure 5 a,b) perform reasonably well ($RMSRE < 5\%$) and the comparison to other cases is not affected by larger deviations outside of this range.

4.1.1 Setup 1: Three Cylindrical Probes

For this setup, three cases are presented in detail. For all probes, a diameter of 0.255 mm is chosen. This is the same as for the m-NLP (Jacobsen et al., 2010). Case 1), consists of one cylinder with 25 mm length (same as for the m-NLP) and two cylinders with 30 mm length. In case 2), a probe of 25 mm is combined with two longer probes of 40 mm. In case 3), one probe is shortened to 10 mm, while the other two are 90 mm long. The voltages for the probes are set on 2.5, 4 and 7.5 V (adapted from the m-NLP). We remind the reader that past attempts at inferring the temperature for such probes have failed, but then the probes had equal length. We can report that also our NN was incapable of inferring temperature for probes when they were of equal length.

The set parameters for case 1) are listed in 1 (first row). The difference in length of the cylinders is only 0.5 cm, which results in a minor $\Delta\beta$ of (0.03). The standard deviation in β is of the same magnitude. However, even such a small difference in length, enables inference of the temperature. In this case the RMSRE is 4.3%, and the PCC is 0.99 for the inferred temperature in relation to the test set temperature, see Figure 5a. Figure 5b shows that the inferred temperatures lie within 4.1% of the IRI ground truth temperatures. This RMSRE is close to the RMSRE for the original test set.

In case 2) the difference in length was increased to 1.5 cm, increasing $\Delta\beta$ to 0.06, see 1 (second row). The RMSRE decreased to 2.4% and the PCC increased to 1. Figure 5c shows less spread in the scatter plot of inferred vs synthetic temperature and the RMSRE value between inferred temperature and IRI temperature data is only 1.3%,see Figure 5d. This is even better than for the original test set.

In case 3), the length difference is even further expanded. Case 3) consists of a very short 1 cm probe and two long 9 cm probes, parameters listed in 1 (third row). The RMSRE in this case is as low as 0.7% and the PCC stays at its maximum, see Figure 5e. The inference of temperature is improved further. The RMSRE is here 0.5%, as shown Figure 5f.

Case 1) shows how a minor difference in probe length enables inference of temperature. In case 2), the precision of the inferred temperatures are improved by increasing the length difference. While case 3) leads to the best results, one may be in favor of case 2), as it shows major improvements compared to case 1) and does not require as much design modifications from the m-NLP as case 3).

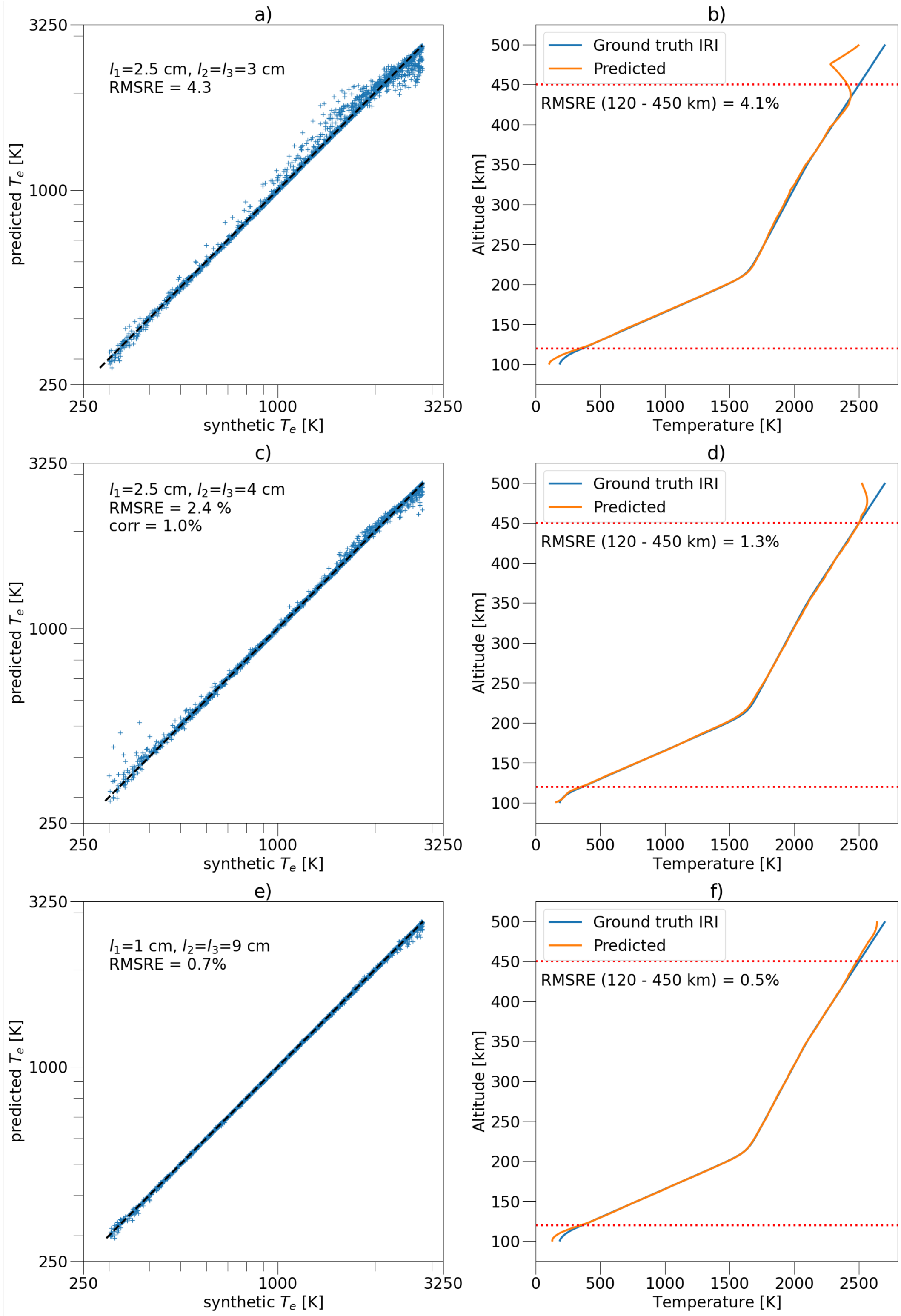

Figure 5. Setup 1), three cylindrical probes: Predicted temperatures versus synthetic temperatures of the test set are shown in form of scatter plots in panel a,c,d. Probe geometry and RMSRE are reported in the plot texts. Altitude profiles of temperature data from IRI are shown as ground truth in blue, and inferred temperature data from probe currents calculated from IRI data are shown in orange in panel b,d,f. The red horizontal lines delimit the range over which the RMSRE reported in the plot, was calculated.

4.1.2 Setup 2: Three Spherical Probes

Spherical probes can also be used to infer temperature, using the same approach. One probe has a different size compared to the other two. In this case, one spherical probe with a radius of 0.5 cm and two spherical probes with radii of 1.5 cm are selected. The voltages for the probes are set on 2.5, 4 and 7.5 V (same as for the cylindrical probes). The parameters are summarized in table 2. For spherical probes β is closer to 1. Here, the $\Delta\beta$ is 0.08. This value lies in between the $\Delta\beta$ of setup 1, case 2 and case 3 (cylindrical probes). The RMSRE between test and inferred temperature is 1.4%, also between the RMSRE of setup 1, case 2 and case 3 (cylindrical probes). This is shown in Figure 6a. Panel b shows the comparison of IRI temperatures and inferred temperature. The RMSRE is 0.7%, lower than for the original test data. The temperature inference performance using spherical probes is comparable to the one of the cylindrical probes.

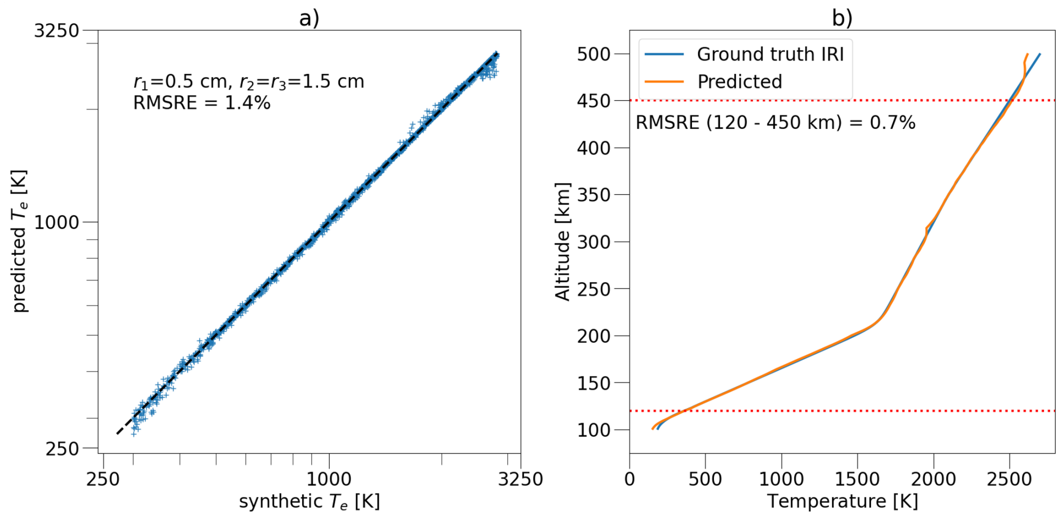

Figure 6. Setup 2), three spherical probes: Predicted temperatures versus synthetic temperatures of the test set are shown in form of scatter plots in panel a. Probe geometry and RMSRE are reported in the plot texts. The altitude profile of temperature data from IRI is shown as ground truth in blue, and inferred temperature data from probe currents calculated from IRI data is shown in orange in panel b. The red horizontal lines delimit the range over which the RMSRE reported in the plot, was calculated.

4.1.3 Setup 3: Combination of four Cylindrical Probes and a Spherical Probe

The same setup of probes as flown on the ICI-2 rocket is chosen to be evaluated in this section, four cylindrical probes and one spherical probe (probe setup: ICI-2) (Jacobsen et al., 2010). In case 1 of this setup the same geometry as for the m-NLP is used, see parameters summarized in table 3 (first row). The radius of the spherical probes is 10 mm, the length of the four cylindrical probes are 25 mm and their diameter is 0.255 mm. The voltages for the cylindrical probes are set on 2.5, 4, 5.5 and 10 V and for the spherical probe 4 V (same as for the ICI-2 probe setup). The geometry difference results in a $\Delta\beta$ of 0.2. This is rather large, compared to the previous studied cases with a maximum $\Delta\beta$ of 0.16 in setup 1, case 3 (cylindrical probes). However, the RMSRE is 79%, giving a PCC of 0.85 between test and inferred data, see Figure 7a. This does not provide a reliable method to infer the electron temperature.

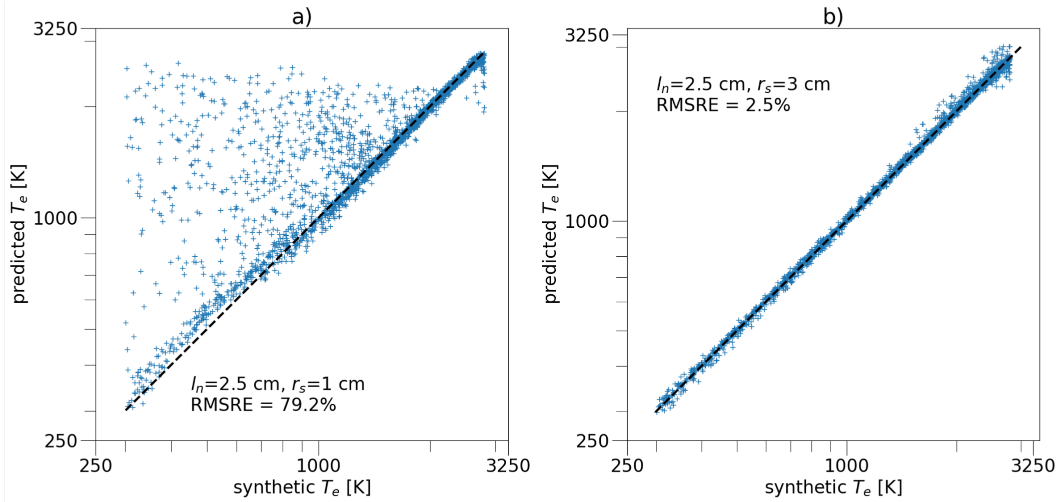

Figure 7. Setup 3), four cylindrical Probes and a spherical probe: Predicted temperatures versus synthetic temperatures of the test set are shown in form of scatter plots in panel a,b. Probe geometry and RMSRE are reported in the plot texts.

In an attempt to improve the inference (case 2), the cylinders have been increased to a size of 70 mm, see table 3 (second row). This increases $\Delta\beta$ to 0.3 and strengthens the PCC to 99%. Nevertheless, the RMSRE remains high, at 22%.

Keeping the length of the cylindrical probes at 25 mm, while adjusting the radius of the spherical probe delivers better results. The Parameters for case 3 are shown in 3 (third row). The $\Delta\beta$ is now 0.03, which is similar to the cases with only spherical or cylindrical probes, we studied previously. The RMSRE between test and inferred data is down to 2.5% and the PCC is at 0.99, see Figure 7b. This is now similar to previous values for other setups for which temperature inference is achieved.

Case 4 uses a setup with cylindrical probes of 25 mm length and a spherical probe of only 3 mm radius. The $\Delta\beta$ is comparably high at 0.27 and in the same range of the first two cases for this setup in which reliable temperature inference was not achieved. In this case however, we achieve similar results as for setup 1, case 3 (cylindrical probes) in which we used long probes of 9 cm. The RMSRE is only 0.8% and the PCC is 1, see Figure 8a. Applying the NN model to currents calculated from IRI data to infer temperature and comparing it to IRI temperature ground truth data, gives a RMSRE of 0.005% within 120-450 km, see Figure 8b. This is the best achievement of all evaluated cases. The setup of case 4 can be easily achieved by modifying the ICI-2 probe setup and simply using a smaller spherical probe.

The geometry in case 1 and 2 did not provide reliable temperature inference. In case 3 and 4 the spherical probe size could be adapted to enable temperature inference. The reason for this could be that in case 3 the radius of the sphere is so large (30 mm), that its dependence of the current on the temperature could be compared to the measurements by a similar size cylindrical probe (here 25 mm). We can also see the similarity when comparing β for the spherical probe and cylindrical probe, see table 3 (third row). For the spherical probe β equals 0.75, and for the cylindrical ones 0.72. Therefore their dependence on temperature is similar and the NN model can predict temperatures. In case 4, the spherical probe radius is 3 mm and corresponding β is 0.99. A cylindrical probe, with small length acts as a sphere. In this case the probe might be so small that it does not matter, whether it is a cylinder or a sphere as the temperature dependence is also similar here. Again, all probes could be considered as cylinders. Thus it may be easier to infer the temperature from only spheres or cylinders or mixed geometries in a limit where they approach another. Future research into why mixed geometry setups fail, and what could be done about it, could be useful. If inference were successful, it might enable rapid temperature inference of past missions not initially designed for it, such as the ICI-2.

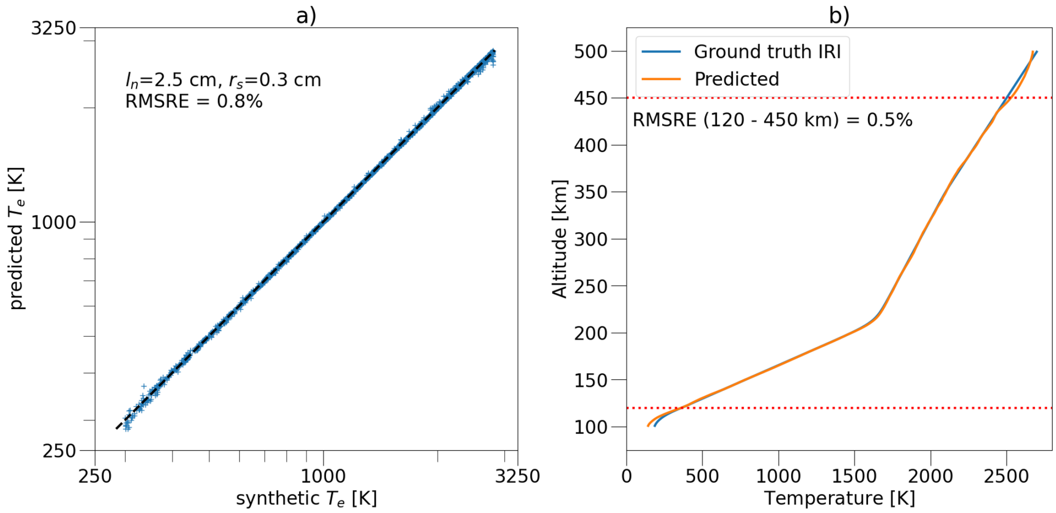

Figure 8. Setup 3), four cylindrical Probes and a spherical probe: Predicted temperatures versus synthetic temperatures of the test set are shown in form of scatter plots in panel a. Probe geometry and RMSRE are reported in the plot texts. The altitude profile of temperature data from IRI is shown as ground truth in blue, and inferred temperature data from probe currents calculated from IRI data are shown in orange in panel b. The red horizontal lines delimit the range over which the RMSRE reported in the plot, was calculated.

4.2 Robustness and Consistency

One method to understand the robustness of our model is to add noise to the system and evaluate its performance. Different noise levels (σ) have been added to the currents calculated from data of the IRI model (using equation 9). First, currents measured by three cylindrical probes (case 2: l_1=3 cm, l_2=l_3=4 cm) are calculated, then, noise is added and again, the temperature is inferred. The probe parameters, noise level and performance parameters are listed in table 4. Above a noise level of $\sigma = 2 \cdot 10^{-6}$ the performance decreases and the RMSRE grows to more than 5% (table 4, third row). As for the presented case with only spherical probes (r_{s1}=0.5 cm,r_{s2}=r_{s3}=1.5 cm), the noise level can be increased to $\sigma = 10^{-5}$ until the RMSRE increases over 3%, see parameters in table 5. Testing the robustness of the setup with four cylindrical probes and one spherical probe (case 4: l_n=2.5 cm, r_s=0.3 cm), a noise level above $\sigma = 10^{-5}$ would increases RMSRE to over 5.4%, see table 6.

Table 4. Parameters for Robustness Evaluation of Probe Setup 1: three cylindrical probes. In the table the probe length (l), bias voltage (V_{b1}), noise level (σ) and parameters to evaluate the temperature inference performance RMSRE and PCC are reported.

l_1[cm]	V_{b1}[V]	$l_2 = l_3$[cm]	V_{b2}[V]	$V_{b3}[V]$	σ	RMSRE[%]	PCC
2.5	4	4	2.5	7.5	10^{-7}	1.7	0.999
2.5	4	4	2.5	7.5	10^{-6}	2.9	0.997
2.5	4	4	2.5	7.5	$2 \cdot 10^{-6}$	5.4	0.986

Table 5. Parameters for Robustness Evaluation of Probe Setup 2: three spherical probes. In the table the probe length (l), bias voltage (V_{b1}), noise level ($d\sigma$) and parameters to evaluate the temperature inference performance RMSRE and PCC are reported.

r_{s1}[cm]	V_{b1}[V]	$r_{s2} = r_{s3}$[cm]	V_{b2}[V]	V_{b3}[V]	σ	RMSRE[%]	PCC
0.5	4	1.5	2.5	7.5	10^{-5}	3	0.997

Table 6. Parameters for Robustness Evaluation of Probe Setup 3: four cylindrical probes and a spherical probe. In the table the probe length (l), bias voltage (V_{b1}), noise level ($d\sigma$) and parameters to evaluate the temperature inference performance RMSRE and PCC are reported.

r_s	V_{b1}	l_n	$V_{b2} - V_{b4}$	σ	RMSRE[%]	PCC
0.3	4	2.5	2.5,4,5.5,10	10^{-5}	5.4	0.989

To prove that the changes to the probe geometry do not sacrifice the ability to infer electron density and floating potential, we also have successfully inferred both of them from the different probe setups. One case is shown in Figure 9 a,b, where the electron density and floating potential were inferred from a setup of cylindrical probes and a spherical probe (case 4: l_n=2.5 cm, r_s=0.3 cm) just as in table 3 (fourth row). The floating potential was inferred from the same NN as the electron temperature (7,041 trainable parameters). However, the electron density was inferred from a network with six dense layers but only 40 nodes each layer (8,481 trainable parameters). The same has been done for the other setups (not shown here).

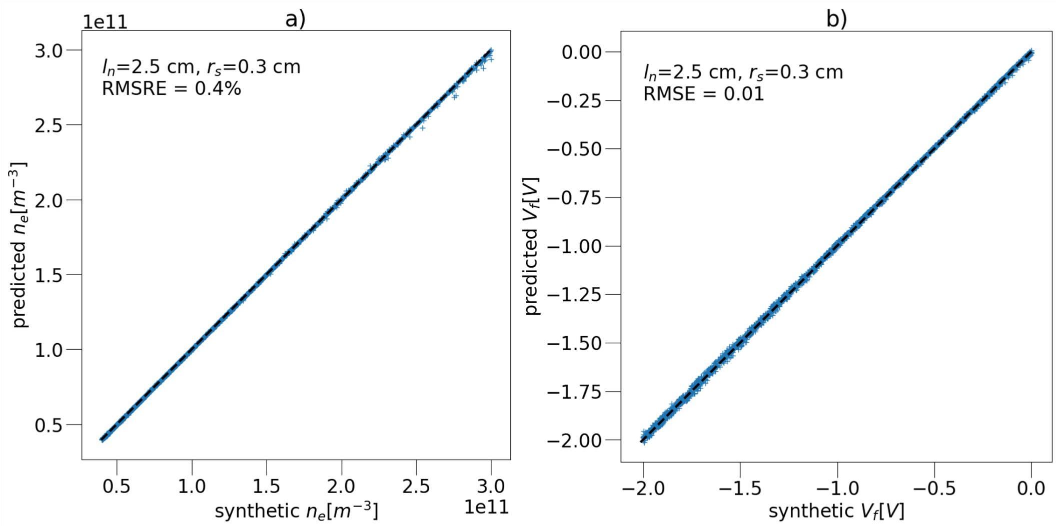

Figure 9. A NN model is applied to electron density and bias voltage to verify that besides the electron temperature, also the other parameters can still be inferred. In panel a, the inferred electron density versus the synthetic electron density of the test set is shown in form of a scatter plot. In panel b, the scatter plot shows the inferred floating potential versus the synthetic floating potential of the test set. The low RMSRE and root mean square error (a different error measure needed to be used here, due to the values between 0-1) demonstrates that the electron density and floating potential can be inferred from this setup. The setup used for this analysis consists of four cylindrical probes (2.5 cm length) and a spherical probe (0.3 cm radius): setup 3, case 4).

5 Discussion and Conclusion

In this work, we showed the first achievement of inferring the electron temperature using fixed-biased Langmuir probes operating in the electron saturation region. This was obtained through considering different probe geometries to achieve temperature sensitivity and then train a NN to predict temperature based on the measured currents. The NN is relatively simple and consists of only 3 layers. The performance of temperature inference has been evaluated with three different setups. At least three probes are required to infer temperature, as the current is dependent on three unknowns: electron density, floating potential and electron temperature. First, a three cylindrical probe setup was assessed in its temperature inference performance. It is found that larger difference in probe length increases the $\Delta\beta$ and with it the performance of inferring temperature, see again table 1. Already minor changes in $\Delta\beta$ enable the temperature inference. When designing an updated m-NLP, a trade-off between probe design factors (e.g. geometry) and temperature inference performance may be preferable. Second, temperature inference performance of a combination of three spherical probes was evaluated. The same behaviour is observed. When introducing a difference in probe size (in this case a different radius), it is shown to be possible and reliable (for $\Delta\beta = 0.08$, with an RMSRE of 1.4%) to reliably infer temperature, see again table 2. Lastly, the inference of temperature from a setup of four cylindrical probes and a spherical probe (ICI-2 setup) was assessed. Given the geometry differences of cylindrical and spherical probes, we only succeeded to reliably (RMSRE $< 5\%$) infer temperature in the limit of a rather large (3 cm radius) or rather small (3 mm radius) spherical probe in combination with the cylindrical probes, see again table 3.

The m-NLP is a frequently used instrument that has an extensive flight heritage on numerous rocket missions, e.g. on ICI-2,3,4 (Jacobsen et al., 2010), ECOMA-7,8,9 (Friedrich et al., 2013), NASA 36.273 MICA (Lynch et al., 2015), Maxidusty 1 and 1b (Antonsen et al., 2019), has also been flown on a satellite mission, e.g. NorSat-1 (Hoang, Clausen, et al., 2018), and is proposed for more future missions e.g. on miniature satellites (Bekkeng et al., 2019) and the International Space Station. From these missions, many studies investigating ionospheric plasmas have been published using the derived electron density from the probes (e.g. Spicher et al., 2015; Lynch et al., 2015; Chernyshov et al., 2018; Jin et al., 2019, 2021; Sinevich et al., 2022, and others). The electron temperature could not be derived, but would add valuable insights to plasma structuring processes, as the electron temperature can be used as a measure of energy injection/dissipation and to characterize a plasma. The instabilities can be directly driven temperature variations or detected by temperature changes (e.g. Perron et al., 2013; Oppenheim & Dimant, 2013; J. Liu et al., 2016, and others).

The efforts of inferring accurate electron temperatures from Langmuir probe configurations (floating and fixed) have existed longer than the m-NLP instrument and are continuously being improved (e.g. Powers, 1966; Hirao & Oyama, 1971; Wrenn et al., 1973; Riccardi et al., 2001; Olowookere & Marchand, 2021; Giono et al., 2021, and others). While Barjatya et al. (2009); Hoang, Røed, et al. (2018); Guthrie et al. (2021) laid the path to using non-linear fits and regression to infer plasma parameters, the key to infer electron temperature is the probe setup to be dependent on it. This was pointed out by Marholm (2020), while Guthrie et al. (2021) stated that only a weak dependence on temperature can be found for the m-NLP. With this stepping stone, we were able to adapt the probe setup accordingly, to introduce temperature sensitivity and successfully infer it.

However, the temperature inference does come with some limitations. We do set certain assumptions on optimal the plasma conditions and are neglecting probe interactions. The presumptions are the same as in Jacobsen et al. (2010). In the probe-design process unwanted potential wake-effects shall be minimized and probe sizing and voltages chosen with regards to encountered plasma conditions, as described in Jao et al. (2022).

Charging effects may occur, and also have been neglected here, but can be taken into consideration when selecting probe bias voltages (Ivarsen et al., 2019). As we added noise to the derived currents, we tested the limitations of the probe setups under conditions of disturbed measurements(Ikezi et al., 1968; G. Liu & Marchand, 2021; Marholm & Darian, 2021). This shows the robustness of our proposed temperature inference method.

In conclusion, we achieved to infer electron temperature from fixed biased multiple Langmuir probe setups. Using three probes, with one length/ geometry different from the other two is the key to enable temperature sensitivity of the probe setup. By changing the length/ radius, the probe setups can be optimized. Finally, different setups can be tested to provide a reliable probe setup to be flown on future satellite or rocket missions. A future adaption of the m-NLP may consider its ability to infer, besides the electron density and floating potential, also the electron temperature. This would enable us to study ionospheric plasma instabilities in higher resolution than before and it would contribute to answer many of the open questions on ionospheric plasmas.

6 Open Research

This paper predominantly makes use of data generated and then post-processed with openly available models and software, such as IRI, Langmuir and TensorFlow. We believe the text is sufficiently detailed to reproduce our results with these codes. Further data used in this paper will be provided upon reasonable request.

Acknowledgments

This work was supported by the European Research Council under the European Union's Horizon 2020 research and innovation programme (grant 866357, POLAR-4DSpace), by the Research Council of Norway (grant 275653) and the Natural Sciences and Engineering Research Council of Canada (NSERC). The numerical simulations were performed on resources provided by Sigma2 - the National Infrastructure for High Performance Computing and Data Storage in Norway, project number NN9299K. This work is a part of the 4DSpace Strategic Research Initiative at the University of Oslo. S.M. and S.A. also acknowledge Øyvind Jensen and the Institute for Energy Technology for permission to complete this research while at IFE.

References

Antonsen, T., Havnes, O., & Spicher, A. (2019). Multi-scale measurements of mesospheric aerosols and electronsduring the maxidusty campaign. doi: https://doi.org/10.5194/amt-12-2139-2019

Barjatya, A., Swenson, C. M., Thompson, D. C., & Wright, K. H. (2009). Invited article: Data analysis of the floating potential measurement unit aboard the international space station. *Review of scientific instruments*, *80*(4), 041301–041301-11. doi: https://doi.org/10.1063/1.3116085

Beghin, C., Hamelin, M., Lebreton, J. P., Vallieres, X., More, J., & Henri, P. (2017, JUL). Electron temperature anisotropy associated to field-aligned currents in the earth's magnetosphere inferred from rosetta mip-rpc observations during 2009 flyby. *Journal of Geophysical Research: Space Physics*, *122*(7), 6964-6977. doi: https://doi.org/110.1002/2017JA024096

Bekkeng, T. A., Helgeby, E. S., Pedersen, A., Trondsen, E., Lindem, T., & Moen, J. I. (2019). Multi-needle langmuir probe system for electron density measurements and active spacecraft potential control on cubesats. *IEEE Transactions on Aerospace and Electronic Systems*, *55*(6), 2951-2964. doi: 10.1109/TAES.2019.2900132

Bekkeng, T. A., Jacobsen, K. S., Bekkeng, J. K., Pedersen, A., Lindem, T., Lebreton, J.-P., & Moen, J. I. (2010, jul). Design of a multi-needle langmuir probe system. *Measurement Science and Technology*, *21*(8), 085903. Retrieved from `https://doi.org/10.1088/0957-0233/21/8/085903` doi: 10.1088/0957-0233/21/8/085903

Bilitza, D. (2018). Iri the international standard for the ionosphere. *Advances in Radio Science*, *16*, 1–11. Retrieved from `https://ars.copernicus.org/articles/16/1/2018/` doi: 10.5194/ars-16-1-2018

Brace, L. H. (1998). Langmuir probe measurements in the ionosphere. In *Geophysical monograph series* (Vol. 102, pp. 23–35). Washington, D. C: American Geophysical Union. doi: https://doi-org.ezproxy.uio.no/10.1029/GM102p0023

Chernyshov, A. A., Spicher, A., Ilyasov, A. A., Miloch, W. J., Clausen, L. B. N., Saito, Y., . . . Moen, J. I. (2018). Studies of small-scale plasma inhomogeneities in the cusp ionosphere using sounding rocket data. *Physics of Plasmas*, *25*(4), 042902. doi: 10.1063/1.5026281

Darian, D., Marholm, S., Mortensen, M., & Miloch, W. J. (2019, jun). Theory and simulations of spherical and cylindrical langmuir probes in non-maxwellian plasmas. *Plasma physics and controlled fusion*, *61*(8), 85025. doi: https://doi.org/10.1088/1361-6587/ab27ff

Dimant, Y. S., Khazanov, G., V, & Oppenheim, M. M. (2021, DEC). Effects of electron precipitation on e-region instabilities: Theoretical analysis. *Journal of Geophysical Research: Space Physics*, *126*(12). doi: https://doi.org/10.1029/2021JA029884

Eltrass, A., & Scales, W. A. (2014, SEP). Nonlinear evolution of the temperature gradient instability in the midlatitude ionosphere. *Journal of Geophysical Research: Space Physics*, *119*(9). doi: https://doi.org/10.1002/2014JA020314

Enengl, F., Kotova, D., Jin, Y., Clausen, L. B. N., & Miloch, W. J. (2022). Ionospheric plasma structuring in relation to auroral particle precipitation. *Earth and Space Science Open Archive*, 29. Retrieved from `https://doi.org/10.1002/essoar.10511323.1` doi: 10.1002/essoar.10511323.1

Fejer, B., & Kelley, M. (1980). Ionospheric irregularities. *Reviews of Geophysics*, *18*(2), 401-454. doi: https://doi.org/10.1029/RG018i002p00401

Friedrich, M., Torkar, K., Hoppe, U.-P., Bekkeng, T.-A., Barjatya, A., & Rapp, M. (2013). Multi-instrument comparisons of d-region plasma measurements. *Annales Geophysicae (1988)*, *31*(1), 135–144.

Giono, G., Ivchenko, N., Sergienko, T., & Brandstrom, U. (2021, JUL). Multipoint measurements of the plasma properties inside an aurora from the spider sounding rocket. *Journal of Geophysical Research: Space Physics*, *126*(7). doi: 10.1029/2021JA029204

Goodfellow, I., Bengio, Y., & Courville, A. (2016). *Deep learning*. MIT Press. (`http://www.deeplearningbook.org`)

Guthrie, J., Marchand, R., & Marholm, S. (2021). Inference of plasma parameters from fixed-bias multi-needle langmuir probes (m-nlp). *Measurement science technology*, *32*(9), 95906.

Hirao, K., & Oyama, K. (1971). Electron-temperature observed with langmuir probe and electron-temperature probe. *JOURNAL OF GEOMAGNETISM AND GEOELECTRICITY*, *23*(2), 161-&. doi: 10.5636/jgg.23.161

Hoang, H., Clausen, L. B. N., Røed, K., Bekkeng, T. A., Trondsen, E., Lybekk, B., . . . Moen, J. I. (2018). The multi-needle langmuir probe system on board norsat-1. , *214*(4), 1. doi: https://doi-org.ezproxy.uio.no/10.1007/s11214-018-0509-2

Hoang, H., Røed, K., Bekkeng, T. A., Moen, J. I., Spicher, A., Clausen, L. B. N., . . . Pedersen, A. (2018). A study of data analysis techniques for the multi-needle langmuir probe. *Measurement Science and Technology*, *29*(6), 065906. doi: 10.1088/1361-6501/aab948

Ikezi, H., Fukiwara, M., & Takayama, K. (1968). Probe noise in quiescent plasmas. *Journal of the physical society of Japan*, *25*(6), 1663-&. doi: https://doi.org/10.1143/JPSJ.25.1663

Ivarsen, M. F., Hoang, H., Yang, L., Clausen, L. B. N., Spicher, A., Jin, Y., ... Lybekk, B. (2019). Multineedle langmuir probe operation and acute probe current susceptibility to spacecraft potential. *IEEE Transactions on Plasma Science*, *47*(8), 3816-3823. doi: 10.1109/TPS.2019.2906377

Jacobsen, K. S., Pedersen, A., Moen, J. I., & Bekkeng, T. A. (2010). A new langmuir probe concept for rapid sampling of space plasma electron density. *Measurement science technology*, *21*(8), 085902–085902. doi: https://doi.org/10.1088/0957-0233/21/8/085902

Jao, C.-S., Marholm, S., Spicher, A., & Miloch, W. J. (2022). Wake formation behind langmuir probes in ionospheric plasmas. *Advances in Space Research*, *69*(2), 856-868. doi: https://doi.org/10.1016/j.asr.2021.11.012

Jin, Y., Clausen, L. B. N., Spicher, A., Ivarsen, M. F., Zhang, Y., Miloch, W. J., & Moen, J. I. (2021). Statistical distribution of decameter scale (50 m) ionospheric irregularities at high latitudes. *Geophysical Research Letters*, *48*(19), e2021GL094794. Retrieved from `https://agupubs.onlinelibrary.wiley.com/doi/abs/10.1029/2021GL094794` doi: https://doi.org/10.1029/2021GL094794

Jin, Y., Moen, J. I., Spicher, A., Oksavik, K., Miloch, W. J., Clausen, L. B. N., ... Saito, Y. (2019). Simultaneous rocket and scintillation observations of plasma irregularities associated with a reversed flow event in the cusp ionosphere. *Journal of Geophysical Research: Space Physics*, *124*(8), 7098-7111. Retrieved from `https://agupubs.onlinelibrary.wiley.com/doi/abs/10.1029/2019JA026942` doi: https://doi.org/10.1029/2019JA026942

Keskinen, M., & SL, O. (1983). Theories of high-latitude ionospheric irregularities-a review. *Radio Science*, *18*(6), 1077-1091. doi: https://doi.org/10.1029/RS018i006p01077

Kingma, D. P., & Ba, J. (2014). *Adam: A method for stochastic optimization.* arXiv. Retrieved from `https://arxiv.org/abs/1412.6980` doi: 10.48550/ARXIV.1412.6980

Laframboise, J. G. (1966). *Theory of spherical and cylindrical langmuir probes in a collisionless maxwellian plasma at rest.* University of Toronto.

Liu, G., & Marchand, R. (2021). Kinetic simulation of segmented plasma flow meter response in the ionospheric plasma. *Journal of Geophysical Research: Space Physics*, *126*(5), e2021JA029120. doi: https://doi.org/10.1029/2021JA029120

Liu, G., Marholm, S., Eklund, A., Clausen, L. B. N., & Marchand, R. (2022). m-nlp inference models using simulation and regression techniques. *Earth and Space Science Open Archive*, 20. doi: https://doi.org/10.1002/essoar.10510978.1

Liu, J., Wang, W., Oppenheim, M., Dimant, Y., Wiltberger, M., & Merkin, S. (2016). Anomalous electron heating effects on the e region ionosphere in tiegcm. *Geophysical Research Letters*, *43*(6), 2351-2358. doi: https://doi.org/10.1002/2016GL068010

Lynch, K. A., Hampton, D. L., Zettergren, M., Bekkeng, T. A., Conde, M., Fernandes, P. A., ... Samara, M. (2015). Mica sounding rocket observations of conductivity-gradient-generated auroral ionospheric responses: Small-scale structure with large-scale drivers. *Journal of Geophysical Research: Space Physics*, *120*(11), 9661-9682. Retrieved from `https://agupubs.onlinelibrary.wiley.com/doi/abs/10.1002/2014JA020860` doi: https://doi.org/10.1002/2014JA020860

Marchand, R. (2012). Ptetra, a tool to simulate low orbit satellite–plasma interaction. *IEEE Transactions on Plasma Science*, *40*(2), 217-229. doi: 10.1109/TPS.2011.2172638

Marchand, R., & Resendiz Lira, P. A. (2017). Kinetic simulation of spacecraft–environment interaction. *IEEE Transactions on Plasma Science*, *45*(4), 535-554. doi: 10.1109/TPS.2017.2682229

Marholm, S. (2020). *The unstructured particle-in-cell method with applications for objects in ionospheric plasmas* (PhD dissertation, University of Oslo). Retrieved from `https://www.duo.uio.no/bitstream/handle/10852/73029/1/PhD-Marholm-2020.pdf`

Marholm, S., & Darian, D. (2021, September). *langmuirproject/langmuir:*. Zenodo. Retrieved from `https://doi.org/10.5281/zenodo.5469073` doi: 10.5281/zenodo.5469073

Marholm, S., & Marchand, R. (2020, Apr). Finite-length effects on cylindrical langmuir probes. *Phys. Rev. Research*, *2*, 023016. doi: https://doi.org/10.1103/PhysRevResearch.2.023016

Moen, J., Oksavik, K., Alfonsi, L., Daabakk, Y., Romano, V., & Spogli, L. (2013). Space weather challenges of the polar cap ionosphere. *Journal of space weather and space climate*, *3*, A02. doi: https://doi.org/10.1051/swsc/2013025

Mott-Smith, H. M., & Langmuir, I. (1926, Oct). The theory of collectors in gaseous discharges. *Phys. Rev.*, *28*, 727–763. doi: https://doi.org/10.1103/PhysRev.28.727

Olowookere, A., & Marchand, R. (2021, JUN). Density-temperature constraint from fixed-bias spherical langmuir probes. *IEEE Transactions on Plasma Science*, *49*(6), 1997-1999. doi: 10.1109/TPS.2021.3076806

Onishchenko, O., Pokhotelov, O., Sagdeev, R., Stenflo, L., Treumann, R., & Balikhin, M. (2004). Generation of convective cells by kinetic alfven waves in the upper ionosphere. *Journal of Geophysical Research: Space Physics*, *109*(A3). doi: https://doi.org/10.1029/2003JA010248

Oppenheim, M. M., & Dimant, Y. S. (2013). Kinetic simulations of 3-d farley-buneman turbulence and anomalous electron heating. *Journal of Geophysical Research: Space Physics*, *118*(3), 1306-1318. doi: https://doi.org/10.1002/jgra.50196

Perron, P. J. G., Noel, J. M. A., Kabin, K., & St-Maurice, J. P. (2013). Ion temperature anisotropy effects on threshold conditions of a shear-modified current driven electrostatic ion-acoustic instability in the topside auroral ionosphere. *Annales Geophysicae*, *31*(3), 451-457. doi: 10.5194/angeo-31-451-2013

Perron, P. J. G., Noël, J.-M. A., & St.-Maurice, J.-P. (2009). Velocity shear and current driven instability in a collisional f-region. *Annales Geophysicae*, *27*(1), 381–394. Retrieved from `https://angeo.copernicus.org/articles/27/381/2009/` doi: https://doi.org/10.5194/angeo-27-381-2009

Powers, R. S. (1966). Comparison of langmuir probe and spectrometric electron temperature measurements. *Journal of Applied Physics*, *37*(10), 3821-&. doi: 10.1063/1.1707933

Riccardi, C., Longoni, G., Chiodini, G., & Fontanesi, M. (2001, JAN). Comparison between fast-sweep langmuir probe and triple probe for fluctuations measurements. *Review of Scientific Instruments*, *72*(1, 2), 461-464. (13th Topical Conference on High-Temperature Plasma Diagnostics, TUCSON, AZ, JUN 18-22, 2000) doi: 10.1063/1.1310578

Sinevich, A. A., Chernyshov, A. A., Chugunin, D. V., Oinats, A. V., Clausen, L. B. N., Miloch, W. J., … Mogilevsky, M. M. (2022). Small-scale irregularities within polarization jet/said during geomagnetic activity. *Geophysical Research Letters*, *49*(8), e2021GL097107. doi: https://doi.org/10.1029/2021GL097107

Spicher, A., Miloch, W. J., Clausen, L. B. N., & Moen, J. I. (2015). Plasma turbulence and coherent structures in the polar cap observed by the ici-2 sounding rocket. *Journal of Geophysical Research: Space Physics*, *120*(12), 10,959-10,978. Retrieved from `https://agupubs.onlinelibrary.wiley.com/doi/`

abs/10.1002/2015JA021634 doi: https://doi.org/10.1002/2015JA021634
Wrenn, G., Clark, D., Raitt, W., & Carlson, H. (1973). Modulation langmuir probe and incoherent scatter radar measurements of the ionospheric electron-temperature. *Journal of Atmospheric and Terrestrial Physics*, *35*(3), 405-413. doi: 10.1016/0021-9169(73)90032-9
Yoon, P. H. (2017). Kinetic instabilities in the solar wind driven by temperature anisotropies. *Reviews of modern plasma physics*, *1*(1). doi: https://doi.org/10.1007/s41614-017-0006-1